Eur. J. Mineral.
2010, **22**, 75–88
Published online November 2009

Precipitation and alteration of coffinite ($USiO_4 \cdot nH_2O$) in the presence of apatite

ARTUR P. DEDITIUS[1,2,*], SATOSHI UTSUNOMIYA[1,3], VÉRONIQUE POINTEAU[1,4] and RODNEY C. EWING[1]

[1] Department of Geological Sciences, University of Michigan, Ann Arbor, MI 48109-1005, USA
[2] CSIRO, Division of Exploration and Mining, 26 Dick Perry Avenue, Kensington, WA 6151, Australia
*Corresponding author, e-mail: artur.deditius@csiro.au
[3] Present address: Department of Chemistry, Kyushu University, Ropponmatsu, 4-2-1, Chuou-ku, Fukuoka-shi, 810–8560, Japan
[4] CEA Saclay, DPC/SECR, 91191 Gif-Sur-Yvette cedex, France

Abstract: A mineral assemblage of coffinite, $USiO_4 \cdot nH_2O$, $n = 0$–2, carbonate-fluorapatite (CFAp) and (Ca, Sr)-(meta)autunite (M-Aut) from the Woodrow Mine, Grants uranium region, New Mexico, has been investigated in order to understand the influence of a P-rich micro-geochemical environment on precipitation of coffinite and its subsequent alteration under oxidizing conditions. Fine-grained coffinite ($\leq$10 µm) precipitated under reducing conditions replacing CFAp, pyrite and aluminosilicates. Electron-microprobe analyses (EMPA) of coffinite indicate limited incorporation of P_2O_5 and CaO, <2.7 and <3.0 wt%, respectively, into the coffinite structure during replacement of CFAp. The chemical formula of coffinite is $(U_{0.95\pm0.09}Ca_{0.15\pm0.02})_{\sum 1.10\pm0.1}(Si_{0.84\pm0.08}P_{0.06\pm0.02})_{\sigma 0.90\pm0.08}$. Analysis by high-angle annular dark-field scanning transmission electron microscopy (HAADF-STEM) revealed that coffinite initially formed as crystals as large as 100 nm at the edges of altered CFAp. Subsequently, infiltration of (Na, Ba, Sr)-rich oxidizing fluids into fractures resulted in precipitation of Sr-rich M-Aut (up to 4 wt% of SrO) at the expense of coffinite and CFAp. High-resolution TEM reveals that Na-rich fluids caused a distortion of the ideal coffinite structure and stabilized amorphous domains that formed due to alpha-decay event radiation damage. Subsequently, the Na-enriched amorphous areas of coffinite were preferentially altered, and secondary porosity formed at the scale of ~1 µm. Porosity also was formed during alteration of CFAp to M-Aut, which facilitated the migration of oxidizing fluids over distances of ~150 µm into CFAp, as evidenced by precipitation of M-Aut. We report, for the first time, the precipitation of coffinite at the expense of apatite and the subsequent alteration of coffinite under P-rich, oxidizing conditions. These results show that micro-scale dissolution of apatite can create conditions conducive to the precipitation of U(IV)- and U(VI)-minerals, leading to the reduced mobility of U-species under both reducing and oxidizing conditions.

Key-words: coffinite, (Ca,Sr)-(meta)autunite, carbonate-fluorapatite, reducing conditions, oxidizing conditions.

1. Introduction

The stability of coffinite, $USiO_4 \cdot nH_2O$, $n = 0$–2, at the nano-scale under reducing and oxidizing conditions received considerable attention recently (*e.g.*, Robit-Pointeau *et al.*, 2006; Cai *et al.*, 2007; Deditius *et al.*, 2008). Coffinite and other U(IV)-silicates are considered to be potentially important phases for U-sequestration during the early stages of spent nuclear fuel (SNF) (~95% of UO_2) alteration in Si-rich ground water under reducing conditions (*e.g.*, Janeczek & Ewing, 1992a and b; Amme *et al.*, 2005; Grambow & Giffaut, 2006). However, there has been only limited investigation of the precipitation and alteration of coffinite at the nano-scale under both reducing and oxidizing conditions. Most of the previous work has been focused on the analysis of variations in the composition of coffinite (*e.g.*, Hansley & Fitzpatrick, 1989; Janeczek & Ewing, 1996). However, Deditius *et al.* (2008) have shown that the presence of other phases, such as organic matter, can have an important effect on the crystal size and composition of coffinite.

In this study we present the results of extensive nano-scale analysis, utilizing a variety of electron microscopy techniques (Utsunomiya & Ewing, 2003), for which coffinite occurs with carbonate-fluorapatite (CFAp) and (Ca,Sr)-(meta)autunite (M-Aut). This provides the basis for understanding the role of P, Ca and Na during the formation and alteration of coffinite. We demonstrate the importance of nano-scale geochemical environments in the formation of coffinite and its subsequent alteration to the U(VI)-phosphates.

2. Coffinite

Coffinite is an orthosilicate, with the general formula of $ABO_4 \cdot nH_2O$, $n = 0$–2, ($I4_1/amd$, $Z = 4$). Coffinite may

0935-1221/10/0022-1990 $ 6.30
DOI: 10.1127/0935-1221/2010/0022-1990
© 2009 E. Schweizerbart'sche Verlagsbuchhandlung, D-70176 Stuttgart

have a range of compositions; the A-site can be occupied with U^{6+}, Zr^{4+}, Th^{4+}, Hf^{4+}, Y^{3+}, REE^{3+}, Ca^{2+}, while the B-site can be occupied with P^{5+}, As^{5+}, V^{5+}, S^{6+}, F^{-} and OH^{-} groups; including the possibility of vacancies at the tetrahedral site (*e.g.*, Stieff *et al.*, 1956; Janeczek & Ewing, 1992a; Burns, 1999; Finch & Hanchar, 2003; Förster, 2006; Deditius *et al.*, 2008).

There have been a number of previous studies that have focused on coffinite that has precipitated from P- and REE-rich fluids in the natural fission reactors at Bangombé, Gabon, where a phosphatian coffinite formed (P-coffinite) (*e.g.*, Janeczek & Ewing, 1996; Bros *et al.*, 2003; Hidaka *et al.*, 2005; Deditius *et al.*, 2009). Most recently HRTEM and HAADF-STEM studies have shown that P-coffinite from Bangombé contains a large fraction of amorphous domains, created by alpha-decay radiation damage, with remnant crystallites of coffinite as large as 10 nm (Deditius *et al.*, 2009). Under oxidizing P-rich conditions, coffinite is altered to Ba-(meta)autunite $Ba[(UO_2)(PO_4)]_2(H_2O)_6$, françoisite-(Nd) $REE(UO_2)_3O(OH)(PO_4)_2(H_2O)_6$ and bassetite $Fe[(UO_2)(PO_4)]_2(H_2O)_8$ (*e.g.*, Janeczek & Ewing, 1996; Jensen *et al.*, 2002; Jerden & Sinha, 2003). Coffinite also altered to (Na)-boltwoodite under oxidizing conditions (Deditius *et al.*, 2008). However, until now, there are few details on the nano-scale characteristics of coffinite that has been formed and altered in a P-rich system under oxidizing conditions.

Importantly, previous the studies have shown that apatite has profound effect on the fate of the migrating U-species (*e.g.*, Finch & Murakami, 1999). Thus, there is a growing interest in the utilization of apatite for the immobilization of oxidized U-species migrating in ground waters utilizing apatite-loaded Permeable Reactive Barriers (PRBs) (*e.g.*, Fuller *et al.*, 2002, 2003). Uranium can be immobilized via surface absorption and subsequent incorporation into apatite structure or as uranyl phosphates, precipitating on the apatite surface (*e.g.*, Ohnuki *et al.*, 2004). In addition, the TEM studies of the vadose zone sediments from Hanford site (USA) revealed immobilization of the migrating UO_2^{2+}-species in the form of nanocrystalline U(VI)-silicate (McKinley *et al.*, 2006; Ilton *et al.*, 2008).

3. Methods

The samples from Woodrow Mine, New Mexico were first examined in polished thin sections by optical and scanning electron microscopy (SEM, Hitachi S3200N equipped with energy dispersive X-ray spectrometry, EDS). The chemical composition of coffinite, M-Aut and CFAp was quantitatively determined by an electron microprobe analyzer (EMPA, Cameca SX100). Accelerating voltage and beam current for coffinite were 20 kV and 40 nA, respectively. The data acquisition time was 120 s. The PAP correction procedure was used to calculate the analyses. The standards used for calibration and detection limits (in ppm) are given in parenthesis: albite for Al($K\alpha$) (55 ppm); $CaTiO_3$ for Ca($K\alpha$) (127) and Ti($K\alpha$) (88); YPO_4 for P($K\alpha$) (120) and Y($L\alpha$) (253); andradite for Si($K\alpha$) (161) and Fe($K\alpha$) (130), MgO for Mg($K\alpha$) (61); synthetic $SrMoO_4$ for Sr($L\alpha$) (407); $BaSO_4$ for S($K\alpha$) (144); cerussite for Pb($M\alpha$) (599); zircon ($ZrSiO_4$) for Zr($L\alpha$) (142); synthetic UO_2 for U($M\beta$) (945); $ThSiO_4$ for Th($M\alpha$) (664); $LaPO_4$ for La($L\alpha$) (256); $CePO_4$ for Ce($L\alpha$) (258).

The analytical conditions for (meta)autunite were: accelerating voltage 15 kV, beam current, 20 nA and data acquisition time was 60 s. The following standards were used for calibration and detection limits (in ppm) are given in parenthesis: albite for Na($K\alpha$) (105); $CaTiO_3$ for Ca($K\alpha$) (288) and Ti($K\alpha$) (88); $CePO_4$ for P($K\alpha$) (260) and Ce($L\alpha$) (656); andradite for Fe($K\alpha$) (304), MgO for Mg($K\alpha$) (87); synthetic $SrMoO_4$ for Sr($L\alpha$) (610); $BaSO_4$ for S($K\alpha$) (158) and Ba($L\alpha$) (745); cerussite for Pb($M\alpha$) (789); zircon ($ZrSiO_4$) for Zr($L\alpha$) (294); synthetic UO_2 for U($M\beta$) (1891); $LaPO_4$ for La($L\alpha$) (652); synthetic $KTaO_3$ for K($K\alpha$) (524) and synthetic ASP for As($L\alpha$) (424).

The acceleration voltage was 15 kV and the beam current was 10 nA during the analyses of CFAp. Special attention was given to the measurements of F and Cl to minimize their anisotropic diffusion in apatite (Stormer *et al.*, 1993). The acquisition time was 20 s and raster size of 5 μm were used to primarily measure F, C, Cl, and Na, while 60 s of acquisition time and spot size of ~1 μm were applied for the other elements (the same analytical conditions and standards were utilized for the measurement of F in coffinite and M-Aut). The concentrations of C in CFAp were measured according to the following procedure: (i) first the C was analyzed in quartz in the same sample in order to evaluate contribution from carbon thin film deposited on the surface of the analyzed samples; the basic value of 2.53 ± 0.44 wt% in the form of CO_2 were obtained; (ii) the concentration of CO_2 in CFAp was analyzed; (iii) finally the average concentration of CO_2 measured on quartz was subtracted from each analysis of CFAp. The standards used for calibration were (detection limits are given parenthesis): synthetic FTOP, PrF_3, EVAP and natural apatite for F($K\alpha$) (1943); synthetic BACL for Cl($K\alpha$) (187); dolomite for C($K\alpha$) (1040); albite for Na($K\alpha$) (157) and Al($K\alpha$) (76); apatite and synthetic $CePO_4$ for P($K\alpha$) (398); apatite for Ca($K\alpha$) (360), andradite for Fe($K\alpha$) (317) and Si($K\alpha$) (106); $BaSO_4$ for Ba($L\alpha$) (688) and S($K\alpha$) (206); synthetic $CePO_4$ for Ce($L\alpha$) (818); synthetic $LaPO_4$ for La($L\alpha$) (812); synthetic $SrMoO_4$ for Sr($L\alpha$) (832); cerussite for Pb($M\alpha$) (1218); synthetic UO_2 for U($M\beta$) (935); arsenopyrite for As($L\alpha$) (256) and synthetic MgO for Mg($K\alpha$) (90).

High-resolution transmission electron microscopy (HRTEM), analytical electron microscopy (AEM), and high-angle annular dark-field scanning transmission electron microscopy (HAADF-STEM) were performed using a JEOL JEM2010F. Spherical coefficient, C_s, is 1.0 mm. In STEM mode, the probe size was 1.0 nm and the collection angle of the HAADF detector was 50–110 mrad. The size of condenser aperture was 20 μm.

4. Geologic setting

The coffinite samples are from Woodrow Mine, New Mexico (Fig. 1a), where U-ore occurs in vertical ''pipe'' that consists of sandstone and montmorillonite-bearing mudstone of the Upper Jurassic Morrison Formation (Fig. 1b) (Moench, 1962). The sandstone is of terrestrial fluvio-lacustrine origin. Coffinite formed during diagenesis of U-ore, when high silica activity was maintained by weathering of feldspars and quartz by organic acids. The close association of coffinite with massive sulfides (Woodrow Mine) or organic matter (Mt. Taylor Mine) indicates that sulfides and/or organic matter were responsible for retarding the migration and subsequent reduction of U^{6+}-species (Goldhaber *et al.*, 1987; Hansley & Fitzpatrick, 1989). Goldhaber *et al.* (1987) suggested that adsorption and subsequent reduction of U(VI)-species occurred at the interface between migrating meteoric waters and reducing saline waters. Coffinite precipitated in the Grants uranium region at relatively low temperatures in the range of 100–130 °C (Hansley & Fitzpatrick, 1989), which well agree with maximal temperature conditions of 130–140 °C reported from other sedimentary deposits (*e.g.*, Janeczek & Ewing, 1992a). Three sources of U have been proposed for U-ore in Grants region: (1) detritus in the host rock; (2) volcanic ash of Jurassic age; and (3) weathered granitic rocks (Goldhaber *et al.*, 1987). The organic material is believed to be the source of P provided during diagenesis for authigenic euhedral apatite that is associated with coffinite (Hansley & Fitzpatrick, 1989). Subsequently, U-ore in Woodrow Mine was partly altered under oxidizing conditions to uranopilite, $(UO_2)_6(SO_4)(OH)_{10}(H_2O)_{12}$, and cuprosklodovskite, $Cu(UO_2)_2(SiO_3OH)_2(H_2O)_6$ (Moench, 1962).

5. Results

5.1. Paragenesis

Major parts of the analysed samples are composed of fine-grained coffinite (<10 μm), which has precipitated in a matrix of preexisting minerals: feldspar + quartz + pyrite + CFAp + roscoelite ± biotite (Fig. 2a, b) under reducing conditions. Coffinite is a primary U-mineral; *i.e.* no uraninite has been found in the analyzed samples. The close association of coffinite and cobaltite, found during TEM studies (see below), confirm contemporaneous precipitation of these two minerals suggested by Moench (1962). The single crystals of CFAp (up to 50 μm long and ~20 μm wide) concentrates as ~100–200 μm-sized layers in sandstone and occasionally they are intergrown with pyrite grains (Fig. 2b–e). The 100–500 μm-sized aggregates of pyrite and quartz were partially dissolved during precipitation of coffinite. Feldspars also underwent dissolution and were replaced by coffinite and/or aggregates of kaolinite (Fig. 2a, c, d). The back-scattered electron (BSE) images reveal that dissolution of CFAp and subsequent precipitation of coffinite started from the outermost parts of the CFAp grains and proceeded inwards (Fig. 2a, b). The analyzed

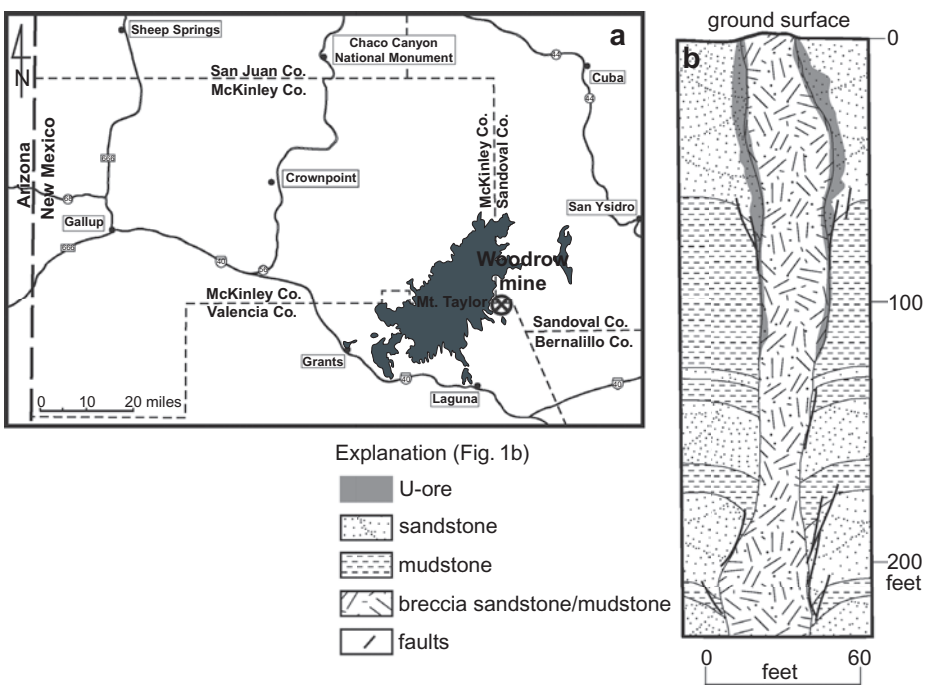

Fig. 1. (a) Locality of studied samples with coffinite, Woodrow Mine, Grants uranium region, New Mexico, USA; (b) simplified section through the Woodrow pipe; after Hilpert & Moench (1960).

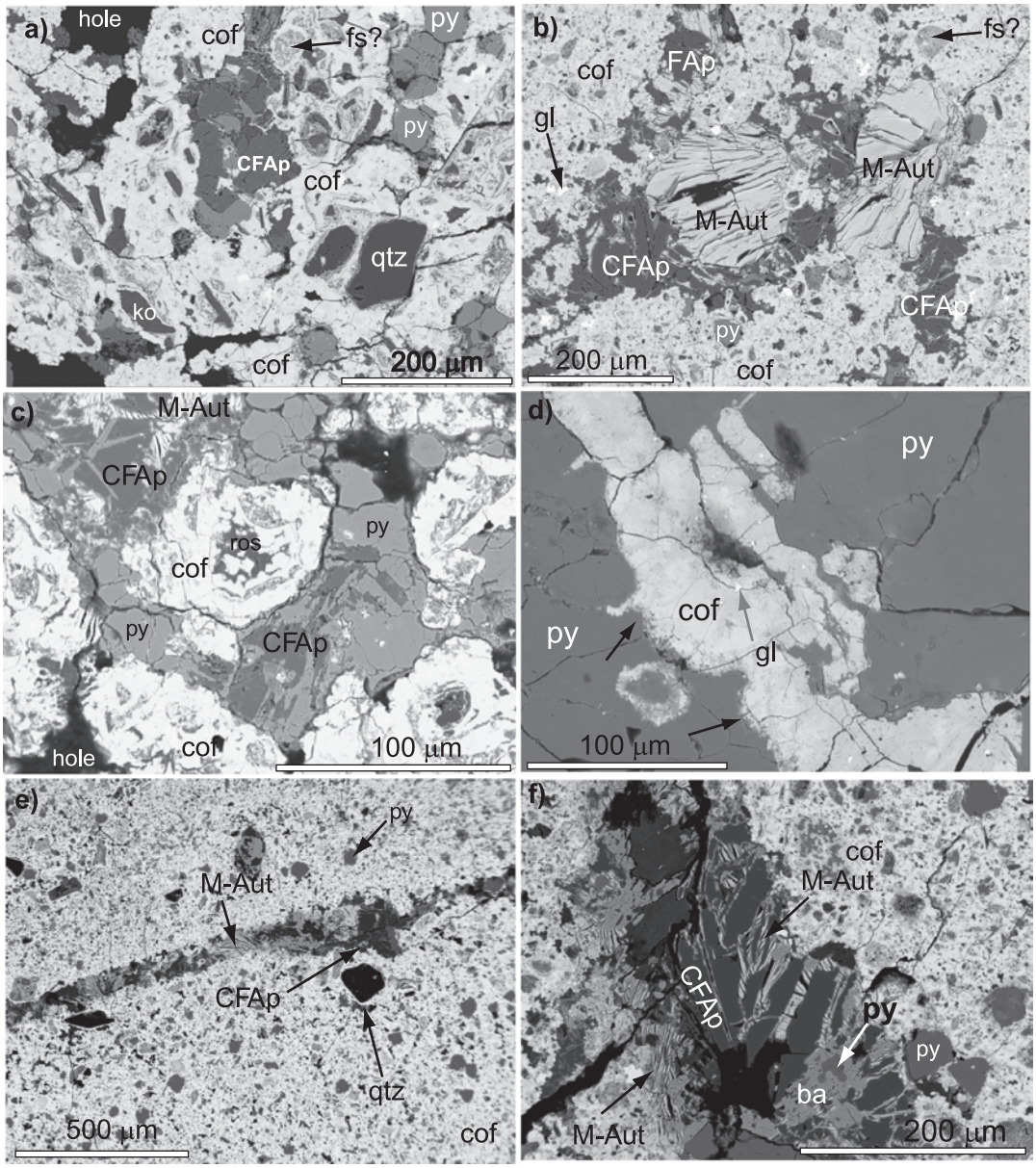

Fig. 2. BSE images of coffinite-bearing sandstone; (a) Coffinite (cof) replacing feldspar (fs) and CFAp – mineral assemblage characteristic for the reducing conditions; (b) platy crystals of M-Aut growing at the expense of coffinite and CFAp; (c) Crystals of CFAp intergrown with pyrite; note that CFAp inside the py vein is not altered by M-Aut; (d) Vein between aggregate of pyrite filled by fine-grained coffinite (cof) and galena (gl); note dissolution of pyrite (py) by coffinite (black arrow); (e) the layer of CFAp and pyrite in the coffinite bearing sandstone; (f) Aggregate of CFAp replaced by M-Aut; note fine-grained barite replacing primary pyrite.

material reveal that oxidizing stage of the U-ore evolution at the Woodrow mine begins with precipitation of M-Aut, which is present as platy crystal as large as 200 µm, at the expense of CFAp and coffinite (Fig. 2b, c, e, f). Aggregates of fine-grained barite replace pyrite also in the vicinity of CFAp crystals (Fig. 2f). In contrast, dissolution of CFAp and precipitation of M-Aut starts from fractures in the aggregates of CFAp and at the boundary between coffinite and CFAp (Fig. 2b, c, e). Alteration of coffinite followed by the precipitation of the uranyl phases was observed at the distance as far as ~150 µm from the CFAp (Figs. 2b and 3a).

5.2. Chemical compositions of coffinite, CFAp and M-Aut

The chemical composition of coffinite reveals trace amounts of compatible non-formula elements like Ca^{2+}, P^{5+} and REE^{3+} (Table 1). Owing to the fine-grained nature and intergrowth with Al-silicates the concentrations of the main constituents in the coffinite vary in the wide ranges; UO_2 from 68.59–78.39 wt%, and SiO_2 from 10.75–18.47 wt%. Analytical total ranges from 87.29 to 96.68 wt%, of which the variation is most probably due to the

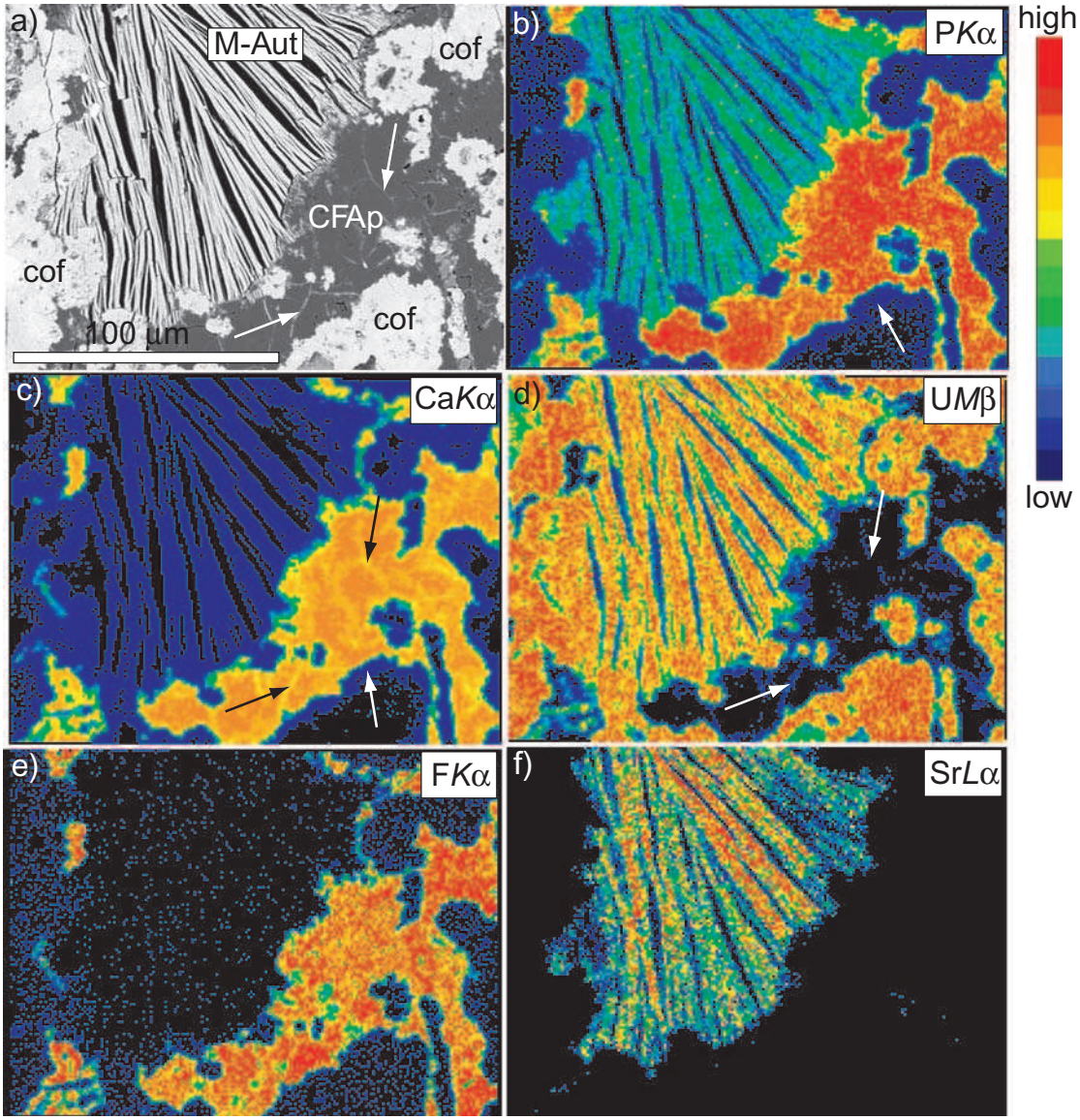

Fig. 3. Elemental mapping of the associated coffinite, M-Aut and CFAp; (a) BSE image of the analyzed area; note white arrows pointing to the areas of CFAp altered to M-Aut – areas depleted in Ca (c) and enriched with U (d); (b) P*K*α; (c) Ca*K*α – the white arrows on (b) and (c) indicates ~10 µm wide rim of coffinite enriched with P and Ca; (d) U*M*β; (e) F*K*α; (f) Sr*L*α.

intergrowths of clays and an H_2O component (Table 1). Special attention was given to the areas where coffinite replaces CFAp in order to investigate the reaction at the interface between coffinite and CFAp. Coffinite in such areas contains CaO in the range from 2.12 to 3.06 wt%, while P_2O_5 reveals ranges from 0.80 to 2.68 wt%. Y_2O_3, Ce_2O_3 and La_2O_3 concentrations, which would have provided for charge balance, are below detection limits (bdl)-0.1 wt%, bdl-0.04 wt% and bdl, respectively. The average chemical formula of coffinite with the standard deviation is: $(U_{0.95\pm0.09}Ca_{0.15\pm0.02})_{\sigma1.10\pm0.1}(Si_{0.84\pm0.08}P_{0.06\pm0.02})_{\sigma0.90\pm0.08}$. Because of the presence of Al-silicates intergrowth, the concentrations of Al_2O_3 is as high as 1.31 wt%, and the mean value of Al_2O_3 is 0.73 ± 0.12 wt% (analyses showing >1.0 wt% of Al_2O_3 were not taken for the further considerations to minimize the contaminations of the impurity mineral). The PbO and FeO contents are as high as 0.69 and 0.4 wt%, respectively. The lack of correlation between PbO, FeO and SO_3, which is <0.21 wt%, indicates that inclusions of galena and pyrite are not present in the area of analysis. Concentration of Na_2O is below 0.22 wt% (Table 1).

The characteristic feature of the chemical composition of M-Aut is the elevated Sr content, up to ~4.0 wt% of SrO (Table 2), which is to our knowledge the highest ever reported for natural uranyl phosphates (Locock *et al.*, 2005; and references therein). The average chemical formula of M-Aut is: $(Ca_{0.55\pm0.06}Sr_{0.26\pm0.04}Mg_{0.03\pm0.02}Fe_{0.01\pm0.007})\{(UO_{2.15\pm0.05})[(P,As)O_4]_{\sigma1.86\pm0.09}\}(H_2O)_6$. The M-Aut contains relatively constant concentrations of the main

Table 1. Representative analyses of coffinite (in wt%).

Sample	1	2	3	4	5	6	7	8	9	10
Na_2O	0.01	0.03	0.04	bdl	0.02	n.a.	n.a.	n.a.	n.a.	n.a.
MgO	0.03	0.02	0.03	0.03	0.02	0.03	0.03	0.05	0.03	0.03
Al_2O_3	0.66	0.63	0.71	0.85	0.74	0.52	0.73	0.60	0.68	0.69
SiO_2	13.65	13.05	14.04	17.39	15.18	10.75	13.16	11.72	14.00	13.99
P_2O_5	0.94	0.89	1.01	1.59	1.36	1.45	1.06	0.73	2.29	2.36
SO_3	0.04	0.05	0.05	0.08	0.02	0.04	0.06	0.05	0.06	0.04
CaO	2.26	2.28	2.13	2.35	2.20	2.85	2.31	2.40	2.91	2.92
TiO_2	n.a.	n.a.	n.a.	n.a.	n.a.	0.06	0.06	0.05	0.06	0.05
FeO	0.24	0.21	0.21	0.15	0.18	0.29	0.25	0.28	0.16	0.21
Y_2O_3	0.04	0.06	0.06	0.05	0.05	bdl	0.03	0.03	0.03	0.03
ZrO_2	n.a.	n.a.	n.a.	n.a.	n.a.	bdl	bdl	bdl	0.02	bdl
La_2O_3	bdl	bdl	bdl	bdl	bdl	bdl	bdl	0.02	bdl	bdl
Ce_2O_3	bdl	0.03	bdl	bdl	bdl	bdl	0.02	bdl	0.02	0.04
PbO	0.47	0.49	0.53	0.30	0.27	0.504	0.51	0.14	0.23	0.24
UO_2	76.32	76.96	74.90	73.16	70.36	78.39	74.38	76.61	70.53	71.41
Total	94.66	94.71	93.71	95.47	90.43	94.93	92.63	92.70	91.02	92.03
Normalized for 4 O^{2-}										
Na	0.001	0.006	0.007	bdl	0.004	n.a.	n.a.	n.a.	n.a.	n.a.
Mg	0.003	0.002	0.003	0.002	0.002	0.003	0.003	0.004	0.002	0.003
Al	0.043	0.044	0.049	0.053	0.050	0.038	0.052	0.045	0.046	0.047
Si	0.807	0.787	0.829	0.925	0.885	0.671	0.797	0.740	0.811	0.804
P	0.047	0.045	0.150	0.072	0.067	0.076	0.055	0.039	0.112	0.115
S	0.002	0.002	0.002	0.003	0.001	0.002	0.003	0.002	0.002	0.002
Ca	0.143	0.147	0.135	0.133	0.137	0.191	0.150	0.162	0.180	0.180
Ti	n.a.	n.a.	n.a.	n.a.	n.a.	0.003	0.003	0.002	0.002	0.002
Fe	0.012	0.011	0.010	0.007	0.009	0.015	0.013	0.015	0.008	0.010
Y	0.002	0.002	0.002	0.001	0.002	bdl	0.001	0.001	0.001	0.001
Zr	n.a.	n.a.	n.a.	n.a.	n.a.	bdl	bdl	bdl	0.001	bdl
La	bdl	bdl	bdl	bdl	bdl	bdl	bdl	0.001	bdl	bdl
Ce	bdl	0.001	bdl	bdl	bdl	bdl	0.001	bdl	0.001	0.001
Pb	0.008	0.008	0.008	0.004	0.004	0.008	0.008	0.002	0.004	0.004
U	1.004	1.032	0.985	0.866	0.913	1.089	1.002	1.077	0.909	0.913
Total cat.	2.086	2.087	2.082	2.067	2.074	2.098	2.085	2.092	2.079	2.080

ThO_2 and F – below detection limits (bdl); n.a. – not analyzed.

components UO_2, P_2O_5, CaO and SrO (Table 2). A small amount of As, <0.23 wt% of As_2O_5, may substitute for P. The M-Aut analyzed in the present sample does not contain Ba, which is commonly reported in the analyses of uranyl phosphates (*e.g.*, Burns, 1999; Finch & Murakami, 1999).

All analyses of CFAp reveal unusually high F-content, varying from 4.95 to 5.66 wt%. The depleted P-content and the excess of F suggest substitution of CO_3F^{3-} ion for PO_4^{3-} tetrahedra (*e.g.*, Pan & Fleet, 2002) (Table 3). The calculated CO_2-content ranges from 3.09 to 5.34 wt%, which are in a good agreement with measured CO_2-content ranging from 3.17 to 5.68 wt% (Table 3). As a consequence, the chemical formula of the CFAp in the present sample is: $(Ca_{4.91\pm0.01}Si_{0.02\pm0.004}Na_{0.01\pm0.005}Sr_{0.01\pm0.002}U_{0.01\pm0.008})_{S4.95\pm0.04}(P_{2.58\pm0.05}C_{0.47\pm0.06}O_4)_{S3.05\pm0.07}F_{S1.37\pm0.06}$. The lower values for P and Ca may be also attributed to the submicrometer-scale alteration of CFAp to M-Aut, which is consistent with analysis of UO_2 concentration in CFAp being as high as 1.72 wt%.

Elemental maps of coffinite associated with CFAp and M-Aut reveal that incorporation of P and Ca into coffinite is limited to the 10 μm-thick layer of coffinite surface adjacent to the CFAp (Fig. 3a–f). The elemental maps and EMPA analyses have a homogeneous distribution of P, Ca and Sr in M-Aut. There is little difference in Ca concentration between coffinite and M-Aut, ~1 wt% of CaO, while the P_2O_5 content in M-Aut is greater (>10 wt%) than that in coffinite. Thus, a large part of P liberated from CFAp is scavenged by M-Aut. Depletion in P and Ca is observed in the outermost part of CFAp grains, ~1–2 μm thick, possibly due to its alteration (Fig. 3b, c). The elemental mapping and spot analyses also reveal that concentrations of F in coffinite and in M-Aut are below detection. M-Aut is the only phase that contains Sr in the present analysis (Fig. 3f).

5.3. HRTEM

Figure 4a–d are HAADF-STEM images and EDS profiles showing the assemblage of non-altered coffinite, roscoelite, cobaltite and CFAp. Coffinite appears to have co-precipitated with cobaltite. The CFAp is extensively altered, and 100 nm-long crystals of U-silicate, most probably coffinite, precipitated at the edges of dissolved

Table 2. Representative analyses of (Ca, Sr)-(meta)autunite (in wt%).

Sample	1	2	3	4	5	6	7	8	9	10
Na_2O	bdl	bdl	bdl	bdl	bdl	bdl	bdl	bdl	0.01	bdl
MgO	0.05	0.07	0.05	0.06	0.05	0.05	0.07	0.04	0.03	0.03
P_2O_5	17.34	16.81	18.11	16.44	16.61	16.13	16.30	16.54	16.28	15.22
SO_3	bdl	bdl	0.03	bdl	0.02	bdl	0.02	bdl	0.02	0.04
K_2O	bdl	bdl	bdl	bdl	bdl	bdl	bdl	bdl	bdl	bdl
CaO	3.78	3.65	3.98	3.72	3.67	3.43	3.77	3.11	3.99	4.38
TiO_2	0.01	bdl	bdl	bdl	bdl	bdl	bdl	bdl	bdl	bdl
FeO	0.06	0.05	0.07	0.02	0.05	0.03	0.06	0.11	0.09	0.14
As_2O_5	0.18	0.23	0.09	0.09	0.08	0.06	0.03	0.02	0.03	0.02
SrO	2.88	2.98	3.12	3.29	3.52	3.48	3.26	3.47	2.33	3.17
BaO	bdl	bdl	bdl	bdl	bdl	bdl	bdl	0.02	bdl	0.02
La_2O_3	0.06	bdl	bdl	bdl	bdl	bdl	bdl	bdl	bdl	bdl
Ce_2O_3	bdl	0.02	bdl	bdl	bdl	bdl	bdl	bdl	bdl	0.02
PbO	0.23	0.15	0.08	bdl	bdl	bdl	bdl	0.06	0.03	0.08
UO_2	75.47	73.37	73.91	75.69	74.11	75.06	73.90	73.74	71.00	72.72
Total	100.05	97.33	99.46	99.35	98.12	98.26	97.42	97.13	93.79	95.84
Normalized for 12 O^{2-}										
Na	bdl	bdl	bdl	bdl	bdl	bdl	bdl	bdl	0.005	bdl
Mg	0.009	0.013	0.010	0.012	0.010	0.010	0.015	0.008	0.001	0.007
P	1.946	1.940	2.014	1.884	1.914	1.876	1.898	1.931	1.945	1.821
S	bdl	bdl	0.003	bdl	0.002	bdl	0.002	bdl	0.003	0.004
K	bdl	bdl	bdl	bdl	bdl	bdl	bdl	bdl	bdl	bdl
Ca	0.538	0.533	0.561	0.539	0.535	0.505	0.555	0.460	0.604	0.664
Ti	0.001	bdl	bdl	bdl	bdl	bdl	bdl	bdl	bdl	bdl
Fe	0.006	0.006	0.007	0.002	0.006	0.004	0.007	0.012	0.010	0.016
As	0.023	0.031	0.012	0.012	0.010	0.008	0.003	0.003	0.003	0.003
Sr	0.221	0.236	0.238	0.258	0.278	0.277	0.260	0.277	0.191	0.260
Ba	bdl	bdl	bdl	bdl	bdl	bdl	bdl	0.001	bdl	0.001
La	0.003	bdl	bdl	bdl	bdl	bdl	bdl	bdl	bdl	bdl
Ce	bdl	0.001	bdl	bdl	bdl	bdl	bdl	bdl	bdl	0.001
Pb	0.008	0.005	0.003	bdl	bdl	bdl	bdl	0.002	0.001	0.003
U	2.102	2.102	2.040	2.152	2.120	2.166	2.135	2.135	2.105	2.159

ZrO_2 and F – below detection limits (bdl).

CFAp (Fig. 4a(arrows), b). This observation is in a good agreement with petrographic studies that show coffinite replacement for CFAp under reducing conditions (Fig. 2a, b). The sequence of alteration in the system including coffinite, M-Aut and CFAp, from reducing to oxidizing conditions, can be seen in Fig. 5. First, coffinite replaced CFAp, and both coffinite and CFAp were altered to M-Aut (Fig. 5a). Secondary porosity, ~1 μm, occurred in coffinite and CFAp at this stage of alteration (Fig. 5a–c). The selected-area electron diffraction pattern (SAED) taken from M-Aut shows diffuse diffraction maxima and a diffuse diffraction halo. This may be due to the low crystallinity of precipitated M-Aut or radiation damage caused by the electron beam during observation. The HAADF-STEM images reveal the presence of a 1 μm-thick layer of U-minerals precipitates at the interface between CFAp and coffinite (Fig. 5a, c). In spite of the extensive corrosion the high-resolution TEM show the perfect ordering of the CFAp structure (Fig. 5d).

Closer views of the reaction front of coffinite alteration under oxidizing conditions are shown in Fig. 6a–c. The low-magnification TEM image shows two areas in different contrast, which is due to the different structure in these areas (Fig. 6a). The darker area reveals the composition of coffinite, while the brighter area is enriched in Na in addition to the coffinite composition (Fig. 6b, c). The boundary between these two regions is the alteration front (Fig. 6a–c). The Fast Fourier Transform (FFT) of the HRTEM image confirms that both areas mainly consist of coffinite. However, the HRTEM image shows a sharp boundary between coffinite and Na-rich coffinite, and the boundary is attributed to the difference in the degree of crystallinity. The coffinite with lower concentrations of Na is the most crystalline with a small fraction of amorphous domains just a few nanometers in size and with lattice fringes that are slightly distorted. In contrast, the amorphous fraction is dominant in the Na-rich coffinite, where nano-crystals of coffinite are present in the amorphous matrix (Fig. 6c – ellipse). The amorphous domains in Na-rich coffinite are interconnected, which provides an infiltration path for a Na-rich fluid during alteration. Coffinite with pores (Fig. 5b and 6c) also reveals elevated Na concentration, indicating that infiltration of the Na-rich fluid into the large volume of amorphous domains is one of the major factors that enhance dissolution of coffinite and formation of the secondary porosity.

Table 3. Representative analyses of carbonate-fluorapatite (in wt%).

Sample	1	2	3	4	5	6	7	8	9	10
CaO	55.67	56.24	55.91	55.71	54.90	55.32	55.84	54.59	55.18	55.14
P_2O_5	36.18	37.11	36.25	36.38	36.69	37.40	38.38	37.59	37.09	37.40
SiO_2	0.07	bdl	bdl	bdl	0.31	0.03	bdl	0.03	bdl	bdl
Al_2O_3	0.04	bdl	0.03	0.01	0.12	0.34	0.02	0.03	bdl	0.1
MgO	0.01	bdl	bdl	bdl	0.02	bdl	0.01	0.01	bdl	bdl
Na_2O	0.04	0.03	0.02	0.02	0.07	0.02	0.10	0.03	0.03	0.08
SO_3	0.01	0.02	0.04	0.03	0.08	0.05	0.05	0.02	0.03	0.08
FeO	0.04	0.02	0.42	0.02	0.35	0.05	0.12	0.06	bdl	0.10
SrO	0.11	0.16	0.21	0.11	0.14	0.16	0.04	0.16	0.10	0.14
UO_2	0.42	0.14	0.22	0.13	0.67	0.20	0.07	1.72	1.26	0.88
La_2O_3	bdl	bdl	0.03	bdl	bdl	bdl	bdl	bdl	bdl	bdl
Ce_2O_3	bdl	bdl	bdl	bdl	bdl	bdl	0.04	bdl	0.07	bdl
Cl	0.02	0.01	bdl	bdl	bdl	bdl	0.01	0.01	0.01	bdl
F	5.17	4.98	5.73	5.25	5.31	5.22	4.95	5.08	5.22	5.01
CO_2	5.13[a]	4.02[a]	4.57[a]	5.34[a]	4.41[a]	4.16[b]	3.09[b]	3.56[b]	4.80[b]	4.17[b]
Total	100.13	100.10	100.12	100.14	100.11	100.11	100.08	100.09	100.12	100.11
Corrected total	94.87	95.98	95.43	94.66	95.59	95.83	96.91	96.44	95.20	96.06
Normalized for eight cations										
Ca	4.882	4.948	4.916	4.874	4.843	4.872	4.932	4.881	4.881	4.887
Si	0.005	bdl	bdl	bdl	0.025	0.002	bdl	0.003	bdl	0.001
Al	0.004	bdl	0.003	0.001	0.012	0.033	0.001	0.003	0.001	0.001
Mg	0.001	bdl	bdl	bdl	0.002	bdl	0.001	0.001	0.001	0.001
Na	0.011	0.007	0.005	0.004	0.018	0.006	0.025	0.010	0.009	0.019
S	0.001	0.001	0.002	0.002	0.005	0.003	0.003	0.008	0.002	0.005
Fe	0.003	0.001	0.028	0.001	0.024	0.004	0.008	0.004	bdl	0.007
Sr	0.005	0.008	0.010	0.005	0.007	0.007	0.002	0.006	0.005	0.007
U	0.008	0.003	0.004	0.002	0.012	0.004	0.001	0.032	0.023	0.016
La	bdl	bdl	0.001	bdl	bdl	bdl	bdl	bdl	bdl	bdl
Ce	bdl	bdl	bdl	bdl	bdl	bdl	bdl	bdl	0.002	bdl
$\sum Me$	4.920	4.968	4.969	4.889	4.948	4.931	4.973	4.958	4.924	4.944
P	2.507	2.580	2.518	2.515	2.557	2.602	2.678	2.656	2.535	2.595
Cl	0.002	0.002	bdl	bdl	bdl	bdl	0.001	0.001	0.001	bdl
F	1.338	1.292	1.486	1.356	1.382	1.357	1.291	1.340	1.364	1.307
C	0.573	0.451	0.512	0.596	0.495	0.467	0.347	0.405	0.541	0.470

[a] CO_2 – measured;
[b] CO_2 – calculated.

6. Discussion

6.1. Precipitation of coffinite in the P-rich environment

The first stage of dissolution of the CFAp, quartz and feldspars is contemporaneous with the precipitation of coffinite. The primary pyrite was the reducing agent of the uranyl complexes in the micro-system (Figs. 2d and 4a). As shown in Fig. 2d, the pyrite surface was corroded in contact with coffinite, which suggests that its surface was potentially responsible for adsorbing and reducing uranyl species (*e.g.*, Fuller *et al.*, 2002) followed by the coffinite precipitation. This observation agrees with results reported by Goldhaber *et al.* (1987). Evidence is provided by Fig. 4a that shows Co-Ni-As-S sulfide, probably cobaltite, covering the associated coffinite. This suggests that the reducing species were also available in the mineralizing U-bearing fluids in the Grants uranium region.

Importantly, the HAADF-STEM results reveal that the surface of the dissolved apatite, CFAp, may also be the preferential site for the precipitation of the U(IV)-mineral, coffinite. Figures 4a and 5a present the first image of coffinite precipitation at the expense of phosphate, in this case CFAp. Based on this result, one could expect that this coffinite accommodates a higher concentration of P, as with the P-coffinite from Bangombé, during replacement reaction (Janeczek & Ewing, 1996; Deditius *et al.*, 2009). However, the P-coffinite at Bangombé precipitated from a solution enriched with P, S and REE (Janeczek & Ewing, 1996). The trivalent REEs are crucial to maintaining charge balance when P^{5+} substitutes for Si^{4+}.

In the present samples, most of the P and Ca were liberated from the altered CFAp into the surrounding environment and coffinite incorporated only <2.7 wt% P_2O_5 and less than ~3.0 wt% of CaO during replacement of CFAp (Table 1). Still such an incorporation of Ca and P in coffinite is limited only to outermost part of coffinite aggregates as thick as ~10 μm in contact with CFAp (Fig. 5a), and P concentration in coffinite decreases by ~1.0 wt% as one moves into the aggregate (Fig. 3a).

Regarding the incorporation mechanism of Ca and P into the coffinite structure, three major, heterovalent

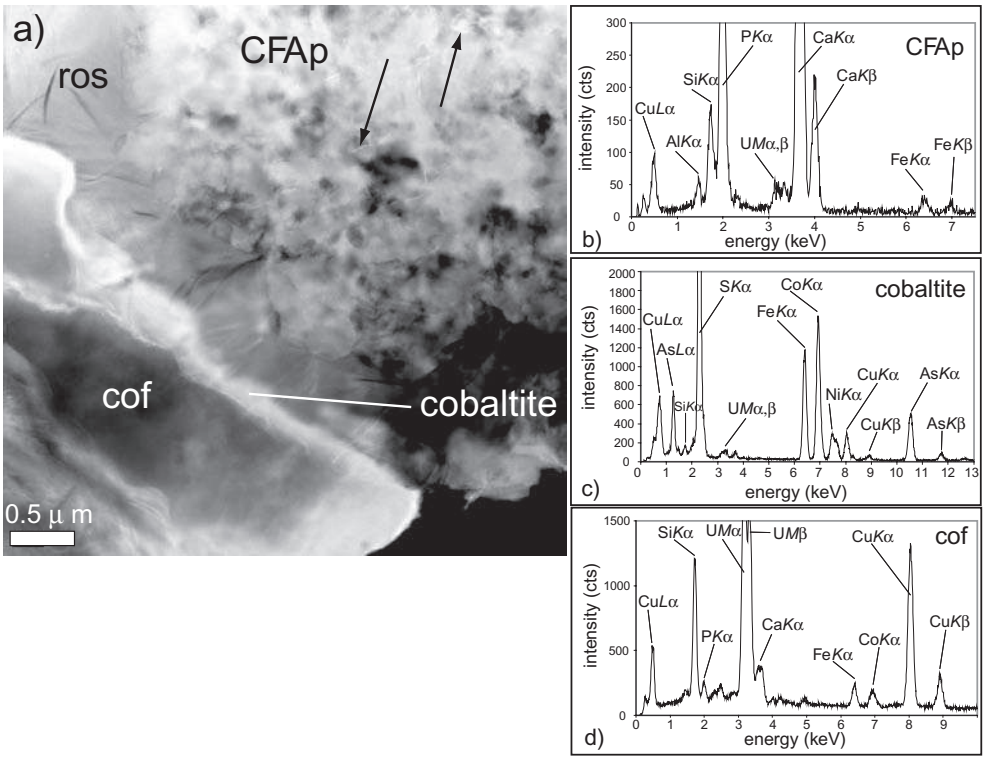

Fig. 4. (a) The HAADF-STEM image of the associated coffinite, cobaltite, roscoelite and CFAp. Note the brighter inclusions of U-silicate growing on the dissolved CFAp (black arrows); (b)–(d) Relevant EDS spectra: (b) U-silicate mineral, coffinite; (c) cobaltite; (d) coffinite.

substitutions were proposed for P-rich coffinite: (i) xenotime-type substitution, $(Y+REE)^{3+} + P^{5+} \Leftrightarrow U^{4+} + Si^{4+}$; and (ii) ningyoite-type substitution, $2Ca^{2+} + 0.8P^{5+} + 0.2\square^{IV} \Leftrightarrow U^{4+} + Si^{4+}$, and (iii) $Ca^{2+} + U^{6+} \Leftrightarrow 2U^{4+}$ (Janeczek & Ewing, 1996). A lack of positive correlation between Ca and U in the present sample indicates that substitution (iii) did not occur in coffinite. However, small amounts of U^{6+}, <0.2 apfu, may occur in coffinite structure with the charge balanced according to the substitution: $U^{4+} + Si^{4+} \Leftrightarrow U^{6+} + [2(OH)^{-}, 0.5\square]$ (Deditius *et al.*, 2008). The relatively high concentrations of Ca suggest that substitution (ii) plays a main role for the coffinite. The first substitution mechanism (i) is very limited, as this coffinite contains only small amount of Y + REE, ~0.1 wt%. Only up to 13 % of the Si in the tetrahedral site is occupied by P in contrast to 54 % of Si position occupied by P in Bangombé coffinite (Deditius *et al.*, 2009). Most recently, Deditius *et al.* (2009) documented that there are two groups of coffinite with respect to the amounts of Ca, P and REE incorporated into the coffinite structure: (i) the (P, Y + REE)-rich coffinite from Bangombé, which may accommodate P and Y + REE as high as 9.84 and 8.64 wt%, respectively; this corresponds to 58 % of Si positions substituted by P and 20 % of U position substituted by Y + REE; and (ii) (P, Y + REE)-poor, Ca-enriched coffinite (other localities), in which less that 15 % of Si and less than 5 % of U positions are substituted by P and Y + REE, respectively; but Ca substitutes as much as 20 % of U positions. These results indicate that the coffinite analyzed in the present study belongs to the (ii) group of coffinite and the low P-content is most probably due to the low-concentrations of Y + REE in the mineralizing fluids. The REE's^{3+} are required in order to balance the excess charge if P^{5+} is incorporated into coffinite structure. This is in good agreement with the previous studies on P-coffinite from Bangombé (*e.g.*, Janeczek & Ewing, 1996; Hidaka *et al.*, 2005), which proposed that P-coffinite precipitates directly from the (P, REE)-rich fluids.

In addition, the HAADF-STEM studies revealed submicrometer scale inclusions of M-Aut in CFAp. This is particularly important for the elevated concentrations of U in apatite associated or replaced by various uranyl phosphates (Fig. 7). Previously reported decreases in the Ca-content (Abd El-Naby & Dawood, 2008) may not indicate the substitution of UO_2^{2+} into apatite structure, but rather the presence of inclusions of uranyl phosphate that are ''invisible'' to SEM or EMPA analysis (Fig. 5c).

6.2. Submicrometer-scale process of coffinite alteration

The HRTEM studies revealed that Na-rich areas of the altered coffinite contain a large amorphous fraction (Fig. 6b, c). The amorphous domains in the Na-rich coffinite areas are overlapping and fully interconnected. This texture is similar to the one observed in P-rich coffinite from Bangombé, Gabon (Deditius *et al.*, 2009) and to the first percolation point in the model of radiation-damaged zircon proposed by Salje *et al.* (1999). On the other hand, thermal impulse, >400 K, could cause significant defect annealing and recrystallization of coffinite (*e.g.*, Lian

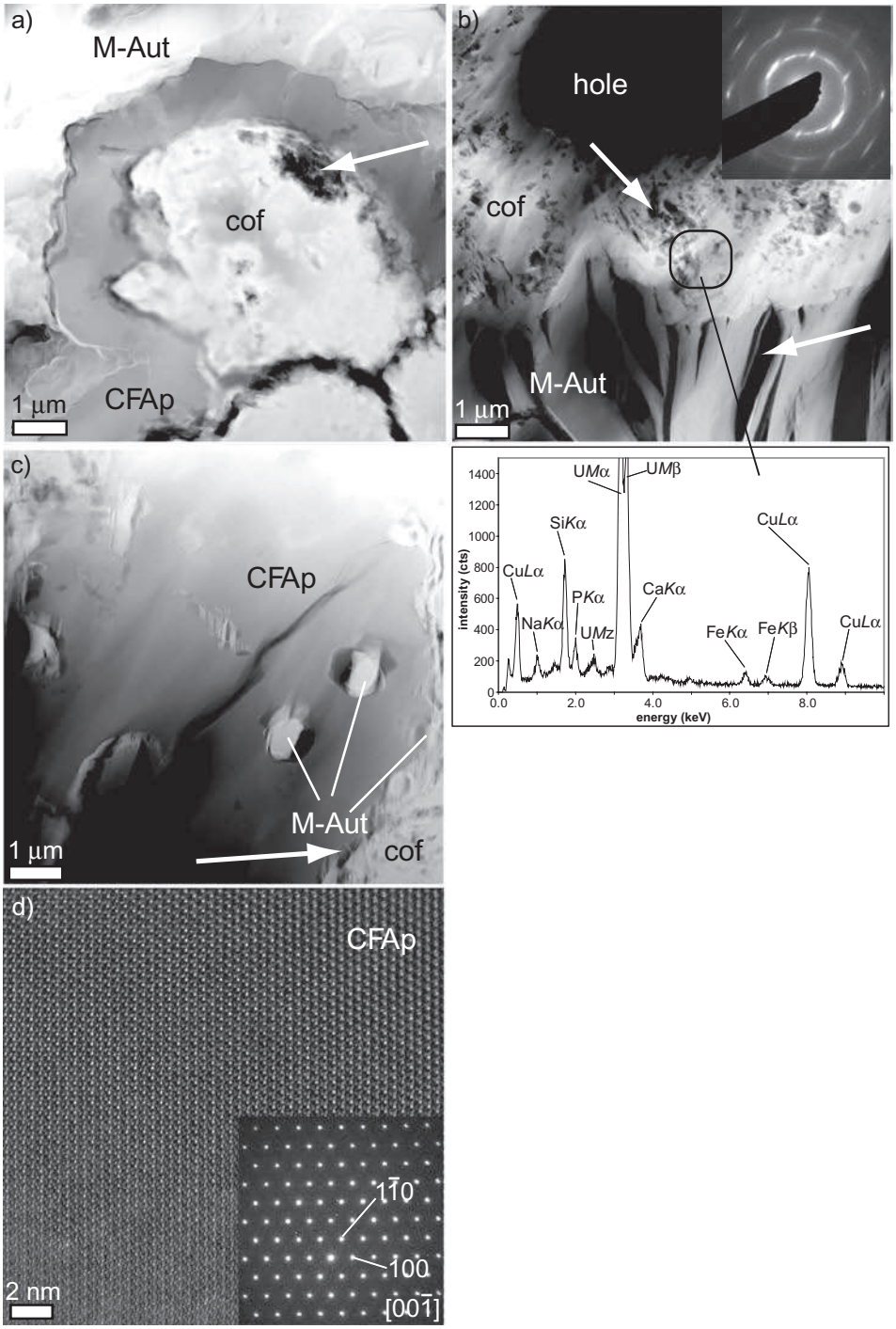

Fig. 5. HAADF-STEM and HRTEM images of the associated coffinite, M-Aut and CFAp; (a) Dissolution of CFAp by coffinite and subsequent alteration of coffinite and CFAp to M-Aut; (b) Alteration of coffinite to M-Aut with associated SAED pattern of M-Aut and EDS analysis of the porous coffinite enriched with Na (rimmed area); the diffused diffraction maxima indicate a low crystallinity of precipitated M-Aut; (c) M-Aut precipitating inside CFAp grains and at the interface between CFAp and coffinite; (a)–(c) Note the extensive formation of porosity; (d) HRTEM image and SAED pattern indicate perfect ordering of CFAp structure in spite of the extensive alteration.

et al., 2009). However, no amorphization was observed in the single crystals of coffinite (the same age) from the Mt. Taylor mine, Grants uranium region, in which the calculated α-decay dose is 4.3–8.5 × 10^{16} alpha decay events/g, which is equivalent to 3.68–7.36 dpa (displacement per atom) (Deditius *et al.*, 2008). For comparison, this dose is much higher than the dose required for the amorphization of zircon, 0.3–0.5 dpa (*e.g.*, Meldrum *et al.*, 1997, 1998). Lian *et al.* (submitted) has shown that synthetic nanocrystalline coffinite is characterized by a much lower activation energy for defect annealing, 0.28, as compared with zircon, thorite and hafnon, >3.3. In addition, the critical

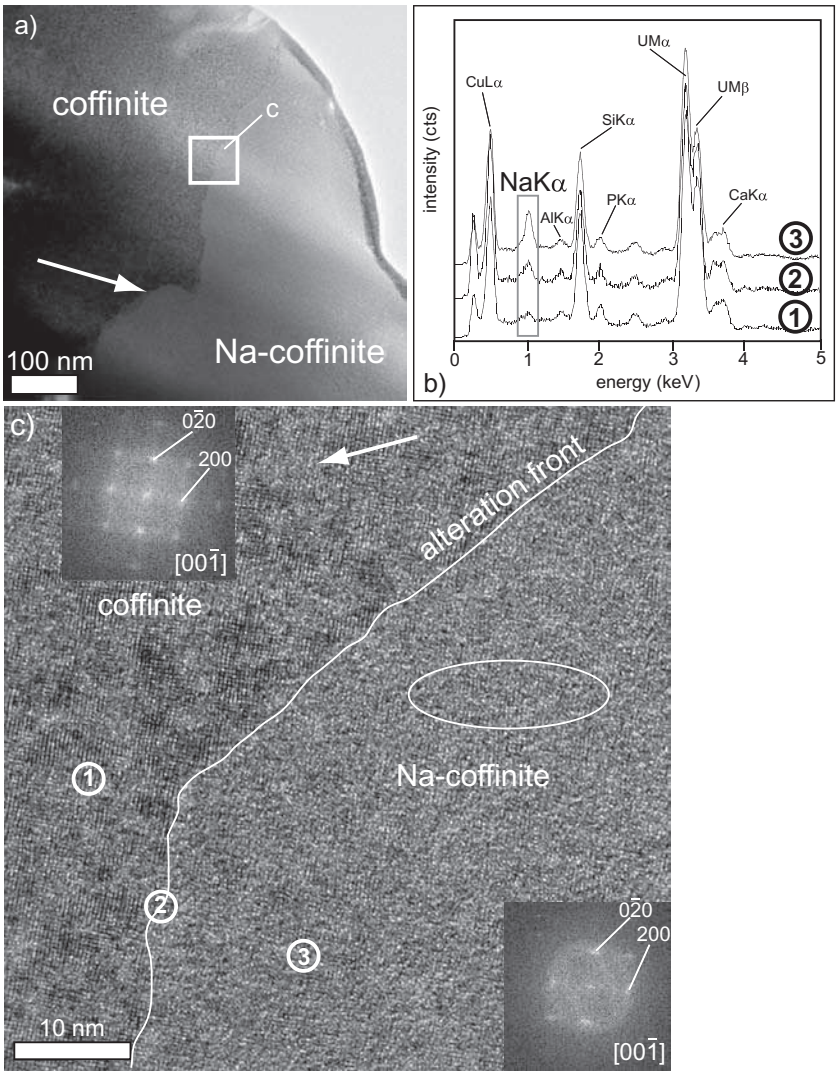

Fig. 6. HRTEM images and EDS analyses of the Na-altered coffinite. (a) Low-magnification TEM image of alteration front (white arrow); white box shows area magnified on the image c; (b)–(c) HRTEM image showing progressive distortion of the coffinite structure with the increase in Na-content (numbers on EDS spectra refer to points on the traverse from coffinite to Na-coffinite); white arrows show an amorphous region in coffinite; the white ellipsoid marks the crystalline ''island'' of coffinite within the heavily distorted Na-coffinite.

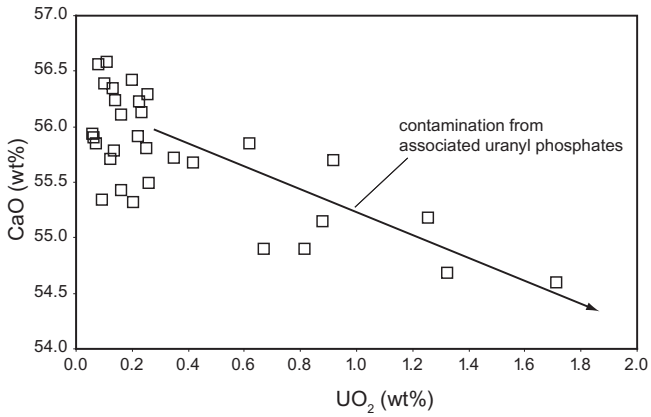

Fig. 7. Plot of the CFAp analyses in the space CaO *vs.* UO_2 (wt%). The arrow indicates the decrease in the CaO content due to the replacement of CFAp by M-Aut.

temperature of coffinite amorphization is low (~608 K), whereas it is >1000 K for the other mentioned orthosilicates. This relatively low temperature of the coffinite annealing, paired with its higher resistance for radiation damage as compared with other orthosilicates, may be responsible for the preservation of the crystalline structure observed in the coffinite from Grants uranium region and to smaller extend in P-coffinite from Bangombé (Fig. 6; and Fig. 5b and 3c–d in Deditius *et al.*, 2008, 2009, respectively). In this sample, the amorphized areas of Na-rich coffinite did not experience temperatures higher than 473 K. At this temperature, amorphous U-silicate (initially coffinite) decomposes to uraninite, which was not found in the studied samples, and SiO_2 (Lian *et al.*, 2009).

Despite of infiltration of Na-rich fluids the relicts of coffinite nano-crystals still remain (Fig. 6c), and the alteration did not result in significant rotation of the relict nano-

crystalline islands, which has been reported for zircon and uraninite (*e.g.*, Ewing *et al.*, 2003; Fayek *et al.*, 2003). In addition, the altered coffinite did not form comb-like textures reported by Fayek *et al.* (2002) for uraninite and coffinite that had altered to calciouranoite. The amorphous domains are likely to be subject to preferential dissolution because the solubility of amorphous material is typically higher than that of the crystalline phase (Weber & Ewing, 2002), resulting in the formation of pores (Fig. 5b). This is evidenced by the close association of the porous areas in coffinite with M-Aut (Fig. 5b), which indicates that Na-infiltration which occurred at the same time as oxidative alteration. Thus, decomposition of coffinite is a coupled effect of penetration of potentially incompatible Na^+ (ionic radius 0.118 nm for VIII-fold coordination; Shannon, 1976) into the damaged coffinite and oxidation of larger U^{4+} (ionic radius 0.100 nm) to smaller U^{6+} (ionic radius 0.086 nm). Incompatibility of Na^+ and U^{6+} in the coffinite structure may also prevent coffinite from recrystallization by subsequent annealing effect. Because of the low temperature thermal history in the present sample (<140 °C), one may pressure that annealing has not occurred. These results on coffinite alteration in Na-rich fluids under oxidizing conditions are consistent with the previous work on alteration of coffinite to Na-boltwoodite, $(Na, K)(UO_2)(SiO_3OH)(H_2O)_{1.5}$ (Deditius *et al.*, 2008), which reported that alteration of coffinite to Na-boltwoodite proceeds: coffinite ⇒ Na-U-silicate (partly or completely amorphous) ⇒ Na-boltwoodite.

6.3. Micro-scale immobilization of U and Sr by phosphates

The mineral assemblage in the present sample provides a rare opportunity to investigate the influence of apatite on U immobilization in the form of less soluble U(IV)-phase coffinite under reducing conditions. In contrast, apatite has been extensively studied as a potential material Permeable Reactive Barriers (PRBs), which is to immobilize the migrating U(VI) species in the groundwaters under ambient oxidizing conditions (*e.g.*, Fuller *et al.*, 2002). Rakovan *et al.* (2002) documented that U^{6+} substitutes for Ca in fluorapatite and is accommodated in the octahedral coordination (<U-O> = 2.06 Å). Studies of uranium deposits at Koongarra (Australia) and Oklo (Gabon) documented replacement of apatite by saléeite (*e.g.*, Murakami *et al.*, 1997; Finch & Murakami, 1999). In experimental studies, the formation of a leached layer in apatite at the grain boundary between apatite and precipitating various uranyl phosphates (autunite, chernikovite) has been described (*e.g.*, Fuller *et al.*, 2002, Ohnuki *et al.*, 2004). Abd El-Naby & Dawood (2008) also found the U-enriched phosphate, which is intermediate in composition between apatite and autunite. All of these studies emphasize the role of local precipitation of the uranyl phosphates at the surface of apatite from fluids that are undersaturated with respect to phosphorous.

Similarly to the mechanism mentioned above, presence of CFAp is one of the major factors that limit the migration of U liberated from coffinite and Sr introduced by oxidizing fluids in the present samples. Probably the concentrations of CaO (<3.0 wt%) and P_2O_5 (<2.7 wt%) in coffinite were not high enough for precipitation of M-Aut inside of the coffinite aggregates (Fig. 2b, e–f). Precipitation of M-Aut only at the vicinity of CFAp indicates supersaturation with respect to M-Aut within the microsystems, which is consistent with a previous experimental study reporting kinetically precipitating autunite on a dissolving surface of fluorapatite with low to neutral pH from the solution undersaturated with respect to autunite (Ohnuki *et al.*, 2004). However, in the case of the samples from Grants uranium region, there is no leached layer of CFAp, as reported by Ohnuki *et al.* (2004). Instead, corrosion rinds on the CFAp surface and inclusions of M-Aut in pores were created during dissolution of CFAp (Fig. 6c). The precipitation of M-Aut as inclusions within CFAp in the present study is very similar to the reported pseudomorphosis of saléeite (Mg-member of autunite) after apatite from the Koongarra U-deposit (Australia) (Murakami *et al.*, 1997; Finch & Murakami, 1999). At the Koongara deposit, primary uraninite was altered by oxidizing fluids and subsequently, after migration, U-species precipitated in the form of saléeite as a result of local supersaturation on the surface of apatite (Murakami *et al.*, 1997). This is consistent with the results of this study that show that M-Aut occurs within the crystals of CFAp without direct spatial contact with coffinite grains. The TEM studies do not confirm precipitation of the ''intermediate phase'', which was previously reported from low-temperature veins in Sela granite (Egypt) (Abd El-Naby & Dawood, 2008). Based on the TEM studies, the shortest distance for the U-species migration, from the leached coffinite to the M-Aut precipitated in CFAp, is 2–5 μm (Fig. 5c).

The formation of the abundant porosity and precipitation of coffinite at the expense of CFAp and M-Aut replacing coffinite and CFAp can be classified as dissolution-precipitation type of reactions (Putnis, 2002; and references therein). The sheet-like shape of M-Aut created fractures between plates of the M-Aut crystals resulting in a relatively large porosity, ~1 μm in size, which provide a path for fluid infiltration (Fig. 3a). In addition, the homogeneous distribution of P, Ca and Sr in M-Aut indicates that the fluid composition remained almost constant for the present mineral assemblage. The alteration of coffinite and CFAp to M-Aut is limited to narrow, ~200 μm, elongated zones that consist of CFAp and/or pyrite (Fig. 2e, f). These zones were probably preferential paths for the migration of oxidizing fluids. There is no alteration of CFAp grains disseminated in the matrix into M-Aut (Fig. 2a). Chernikovite, $(H_3O)_2(UO_2)_2(PO_4)_2 \cdot 6H_2O$, often occurs as an alteration product of apatite in batch experiments (Fuller *et al.*, 2002). Chernikovite was not observed in the analyzed samples. However, its local precipitation cannot be ruled out, especially when it occurs as microcrystalline inclusions in or on the surface of CFAp (Fig. 5c).

7. Conclusions

Coffinite precipitated at the expense of CFAp in two ways: (i) nucleation on the dissolved crystals of CFAp; and (ii) direct replacement reaction. Calcium and P replaced no more than 17 and 8 % of the U and Si, respectively at the outermost 10 µm of coffinite aggregates. This is due to the very low concentrations of REE in the coffinite that would be critical to providing for charge balance. Coffinite is the source of uranium during alteration to Sr-rich M-Aut under the oxidizing conditions. The altering Na-rich fluids attacked coffinite, enhanced disordering and prevented recrystallization of coffinite structure by thermal annealing. That is, it can be considered that the amorphous domains were stabilized by the presence of Na.

There are four main paths of fluid migration in the present samples: (i) the interface between minerals, for example coffinite-CFAp interface; (ii) the amorphous nano-channels developed in coffinite; (iii) the nano- and micro-porosity formed by dissolution of CFAp and coffinite; and (iv) the interlayer channels between platy crystals of M-Aut. The M-Aut precipitated at the interface between dissolving coffinite and CFAp as well as in the secondary porosity within the CFAp, implying that U(VI)-species have migrated as far as 2.5 µm before they were immobilized by the formation of uranyl phosphate. The M-Aut precipitated only at the surface of CFAp, most probably due to local supersaturation. In this sample, the only uranyl phase as a result of coffinite alteration was M-Aut near CFAp, and the sulfides remained stable. Therefore, it can be concluded that oxidizing conditions occur locally at the micro-scale in the grain boundaries of coffinite and CFAp. This study demonstrates that the surface of the unstable, corroded apatite provides suitable conditions for the attenuation of U and the subsequent precipitation of U-minerals under reducing and oxidizing conditions. Precipitation of the Sr-rich M-Aut on the surface of CFAp suggests that relatively insoluble uranyl phosphates can sequester divalent radionuclides, such as ^{90}Sr.

Acknowledgements: The authors thank Carl Henderson and Eric Essene for discussion and guidance on the analytical procedure for the EMPA analyses conducted at the Electron Microbeam Analysis laboratory (EMAL) of University of Michigan. Authors are grateful to Carlos Ayora and two anonymous reviewers for the constructive comments that improve the quality of the article. This work was supported by the Office of Basic Energy Sciences (DE-FG02-06ER15783). Financial support (Grant-in-Aid for Young Scientists) was also provided by Japan Society of the Promotion of Science (JSPS).

References

Abd El-Naby, H.H. & Dawood, Y.H. (2008): Natural attenuation of uranium and formation of autunite at the expense of apatite within an oxidizing environment, south Eastern Desert of Egypt. *Appl. Geochem.*, **23**, 3741–3755.

Amme, M., Wiss, T., Thiele, H., Boulet, P., Lang, H. (2005): Uranium secondary phase formation during anoxic hydrothermal leaching processes of UO_2 nuclear fuel. *J. Nucl. Mat.*, **341**, 209–223.

Bros, R., Hidaka, H., Kamei, G., Ohnuki, T. (2003): Mobilization and mechanisms of retardation in the Oklo natural reactor zone 2 (Gabon)-interferences from U, REE, Zr, Mo and Se isotopes. *Appl. Geochem.*, **18**, 1807–1824.

Burns, P.C. (1999): The crystal chemistry of uranium. *in* ''Uranium: Mineralogy, Geochemistry and the Environment'', P.C. Burns & B. Finch, eds. *Rev. Mineral. Geochem.*, **38**, p. 23–90.

Cai, C., Dong, H., Li, H., Xiao, X., Ou, G., Zhang, C. (2007): Mineralogical and geochemical evidence for coupled bacterial uranium mineralization and hydrocarbon oxidation in the Shashagetai deposit, NW, China. *Chem. Geol.*, **236**, 167–179.

Deditius, A.P., Utsunomiya, S., Ewing, R.C. (2008): The chemical stability of coffinite, $USiO_4 \cdot nH_2O$; $0<n<2$, associated with organic matter: A case study from Grants uranium region, New Mexico, USA. *Chem. Geol.*, **251**, 33–49.

Deditius, A.P., Utsunomiya, S., Wall, M.A., Pointeau, V., Ewing, R.C. (2009): Structure and chemical composition of P-coffinite from the natural fission reactor at Bangombé, Gabon. *Am. Mineral.*, **94**, 827–836.

Ewing, R.C., Meldrum, A., Wang, L.M., Weber, W.J., Corrales, R.L. (2003): Radiation damage in zircon. *in* ''Zircon'', J.M. Hanchar & P.W.O. Hoskin, eds. *Rev. Mineral. Geochem.*, **53**, 387–425.

Fayek, M., Harrison, T.M., Ewing, R.C., Grove, M., Coath, C.D. (2002): O and Pb isotopic analyses of uranium minerals by ion microprobe and U-Pb ages from the Cigar Lake deposit. *Chem. Geol.*, **185**, 205–225.

Fayek, M., Utsunomiya, S., Ewing, R.C., Riciputi, L.R., Jensen, K.A. (2003): Oxygen isotopic composition of nano-scale uraninite at the Oklo-Okélobongo natural fission reactors, Gabon. *Am. Mineral.*, **88**, 1583–1590.

Finch, R.J. & Hanchar, J.M. (2003): Structure and chemistry of zircon and zircon group minerals. *in* ''Zircon'', J.M. Hanchar & P.W.O. Hoskin, eds. *Rev. Mineral. Geochem.*, **53**, 1–26.

Finch, R.J. & Murakami, T. (1999): Systematics and paragenesis of uranium minerals. *in* ''Uranium: Mineralogy, Geochemistry and the Environment'', P.C. Burns & B. Finch, eds. *Rev. Mineral. Geochem.*, **38**, 91–179.

Förster, H.-J. (2006): Composition and origin of intermediate solid solutions in the system thorite-xenotime-zircon-coffinite. *Lithos*, **88**, 35–55.

Fuller, C.C., Bargar, J.R., Davis, J.A., Piana, M.J. (2002): Mechanisms of uranium interactions with hydroxyapatite: Implications for groundwater remediation. *Environ. Sci. Technol.*, **36**, 158–165.

Fuller, C.C., Bargar, J.R., Davis, J.A. (2003): Molecular scale characterization of uranium sorption by bone apatite materials for a permeable reactive barrier demonstration. *Environ. Sci. Technol.*, **37**, 4642–4649.

Goldhaber, M.B., Hemingway, B.S., Mohagheghi, A., Reynolds, R.L., Northrop, H.R. (1987): Origin of coffinite in sedimentary rocks by a sequential adsorption-reduction mechanism. *Bull. Minéral.*, **110**, 131–144.

Grambow, B. & Giffaut, E. (2006): Coupling of chemical processes in the near field. *Mat. Res. Soc. Symp. Proc.*, **932**, 55–66.

Hansley, P.L. & Fitzpatrick, J.J. (1989): Compositional and crystallographic data on REE-bearing coffinite from the Grants uranium region, northwestern New Mexico. *Am. Mineral.*, **74**, 263–270.

Hidaka, H., Janeczek, J., Skomurski, F.N., Ewing, R.C., Gauthier-Lafaye, F. (2005): Geochemical fixation of rare earth elements into secondary minerals in sandstones beneath a natural fission reactor at Bangombé, Gabon. *Geochim. Cosmochim. Acta*, **69**, 685–694.

Hilpert, L.S. & Moench, R.H. (1960): Uranium deposits of the southern part of the San Juan Basin, New Mexico. *Econ. Geol.*, **55**, 429–464.

Ilton, E.S., Quafoku, N.P., Liu, C., Moore, D.A., Zachara, J.M. (2008): Advective removal of intraparticle uranium from contaminated vadose zone sediments, Hanford, U.S. *Environ. Sci. Technol.*, **42**, 1565–1571.

Janeczek, J. & Ewing, R.C. (1992a): Coffinitization – a mechanism for the alteration of UO_2 under reducing conditions. *Mat. Res. Soc. Symp. Proc.*, **257**, 497–504.

—, — (1992b): Dissolution and alteration of uraninite under reducing conditions. *J. Nucl. Mat.*, **190**, 157–173.

—, — (1996): Phosphatian coffinite with rare earth elements and Ce-rich françoisite-(Nd) from sandstone beneath a natural fission reactor at Bangombé, Gabon. *Mineral. Mag.*, **60**, 665–669.

Jensen, K.A., Palenik, C.S., Ewing, R.C. (2002): U^{6+} phases in the weathering zone of the Bangombé U-deposit: Observed and predicted mineralogy. *Radiochim. Acta*, **90**, 761–769.

Jerden, J.L. & Sinha, A.K. (2003): Phosphate based immobilization of uranium in an oxidizing bedrock aquifer. *Appl. Geochem.*, **18**, 823–843.

Lian, J., Zhang, J.M., Pointeau, V., Zhang, F.X., Lang, M.K., Lu, F.Y., Poinssot, C., Ewing, R.C. (2009): Response of synthetic coffinite to energetic ion beam irradiation. *J. Nucl. Mat.*, **393**, 481–486.

Locock, A.J., Burns, P.C., Flynn, T.M. (2005): Structures of strontium- and barium-dominant compounds that contain the autunite-type sheet. *Can. Mineral.*, **43**, 721–733.

McKinley, J.P., Zachara, J.M., Liu, C., Heald, S.C., Prenitzer, B.I., Kempshall, B.W. (2006): Microscale controls on the fate of contaminant uranium in the vadose zone, Hanford site, Washington. *Geochim. Cosmochim. Acta*, **70**, 1873–1887.

Meldrum, A., Boatner, L.A., Ewing, R.C. (1997): Displacive radiation effects in the monazite- and zircon-structure orthophosphates. *Phys. Rev. B*, **56**, 13805–13814.

Meldrum, A., Zinkle, S.J., Boatner, L.A., Ewing, R.C. (1998): A transcient liquid-like phase in the displacement cascades of zircon, hafnon and thorite. *Nature*, **395**, 56–58.

Moench, R.H. (1962): Properties and paragenesis of coffinite from the Woodrow mine, New Mexico. *Am. Mineral.*, **47**, 26–33.

Murakami, T., Ohnuki, T., Isobe, H., Sato, T. (1997): Mobility of uranium during weathering. *Am. Mineral.*, **82**, 888–899.

Ohnuki, T., Kozai, N., Samadfam, M., Yasuda, R., Yamamoto, S., Narumi, K., Naramoto, H., Murakami, T. (2004): The formation of aututnite ($Ca(UO_2)_2(PO_4)_2 \cdot nH_2O$) within the leached layer of dissolving apatite: incorporation mechanism of uranium by apatite. *Chem. Geol.*, **211**, 1–14.

Pan, Y. & Fleet, M.E. (2002): Compositions of the apatite-group minerals: substitutions mechanisms and controlling factors. *in* ''Phosphates: Geochemical, Geobiological, and Materials Importance'', M.J. Kohn, J. Rakovan, J.M. Hughes, eds. *Rev. Mineral. Geochem.*, **48**, 13–49.

Putnis, A. (2002): Mineral replacement reactions: from macroscopic observations to microscopic mechanisms. *Mineral. Mag.*, **66**, 689–708.

Rakovan, J., Reeder, R.J., Elzinga, E.J., Cherniak, D.J., Tait, C.D., Morris, D.E. (2002): Structural characterization of U(VI) in apatite by X-ray absorption spectroscopy. *Environ. Sci. Technol.*, **36**, 3114–3117.

Robit-Pointeau, V., Poinssot, C., Vitorage, P., Grambow, B., Cui, D., Spahiu, K., Catalette, H. (2006): Assessment of the relevance of coffinite formation within the near-field environment of spent nuclear fuel geological disposals. *Mat. Res. Soc. Symp. Proc.*, **932**, 489–496.

Salje, E.K.H., Chrosch, J., Ewing, R.C. (1999): Is ''metamictization'' of zircon a phase transition? *Am. Mineral.*, **84**, 1107–1116.

Shannon, R.D. (1976): Revised effective ionic radii and systematic studies of interatomics distances in halides and chalcogenides. *Acta Crystallogr.*, **A32**, 751–767.

Stieff, L.R., Stern, T.W., Sherwood, A.M. (1956): Coffinite, a uranous silicate with hydroxyl substitution: A new mineral. *Am. Mineral.*, **41**, 675–688.

Stormer, J.C., Pierson, M.L., Tacker, R.C. (1993): Variation of F and Cl X-ray intensity due to anisotropic diffusion in apatite during electron microprobe analysis. *Am. Mineral.*, **78**, 641–648.

Utsunomiya, S. & Ewing, R.C. (2003): Application of high-angle annular dark field scanning transmission microscopy, scanning transmission electron microscop-energy dispersive X-ray spectrometry, and energy-filtered transmission electron microscopy to the characterization of nanoparticles in the environment. *Environ. Sci. Technol.*, **37**, 786–791.

Weber, W.J. & Ewing, R.C. (2002): Radiation effects in crystalline oxide host phases for the immobilization of actinides. *Mat. Res. Soc. Symp. Proc.*, **713**, 443–454.

Received 27 April 2009
Modified version received 23 August 2009
Accepted 18 September 2009